Letter

Selective excitation of superconducting qubits with a shared control line through pulse shaping

R. Matsuda,[1,2,*,†] R. Ohira,[3,*,‡] T. Sumida,[3] H. Shiomi,[2,3] A. Machino,[1,2] S. Morisaka,[2,3] K. Koike,[4] T. Miyoshi,[2,3,4] Y. Kurimoto,[3] Y. Sugita,[3] Y. Ito,[3] Y. Suzuki,[5] P. A. Spring,[6] S. Wang,[6] S. Tamate,[6] Y. Tabuchi,[6] Y. Nakamura,[6,7] K. Ogawa,[2] and M. Negoro[2,3]

[1]*Graduate School of Engineering Science, The University of Osaka, 1-3 Machikaneyama, Toyonaka, Osaka 560-8531, Japan*

[2]*Center for Quantum Information and Quantum Biology, The University of Osaka, 1-2 Machikaneyama, Toyonaka, Osaka 560-0043, Japan*

[3]*QuEL, Inc., Hachioji ON Building 5F, 4-7-14 Myojincho, Hachioji, Tokyo, Japan*

[4]*e-trees.Japan, Inc., Daiwaunyu Building 2F, 2-9-2 Owadamachi, Hachioji, Tokyo 192-0045, Japan*

[5]*NTT Computer and Data Science Laboratories, NTT Corporation, Musashino 180-8585, Japan*

[6]*RIKEN Center for Quantum Computing, Wako, Saitama 351-0198, Japan*

[7]*Department of Applied Physics, Graduate School of Engineering, The University of Tokyo, 7-3-1 Hongo, Bunkyo-ku, Tokyo 113-8656, Japan*

(Received 23 January 2025; revised 10 September 2025; accepted 5 December 2025; published 6 January 2026)

In conventional architectures of superconducting quantum computers, each qubit is connected to its own control line, leading to a commensurate increase in the number of microwave lines as the system scales. Frequency-multiplexed qubit control addresses this problem by enabling multiple qubits to share a single microwave line. However, it can cause unwanted excitation of nontarget qubits, especially when the detuning between qubits is smaller than the pulse bandwidth. Here, we propose a selective-excitation-pulse (SEP) technique that suppresses unwanted excitations by shaping a drive pulse to create null points at nontarget qubit frequencies. In a proof-of-concept experiment with three fixed-frequency transmon qubits, we demonstrate that the SEP technique achieves single-qubit gate fidelities comparable to those obtained with conventional Gaussian pulses while effectively suppressing unwanted excitations in nontarget qubits. These results highlight the SEP technique as a promising tool for enhancing frequency-multiplexed qubit control.

DOI: 10.1103/xw1s-dt16

Introduction. A notable challenge in scaling up superconducting quantum processors is the wiring scheme, which imposes severe space constraints within a refrigerator and generates passive heat loads that can exceed the cooling capacity when the number of qubits is high [1]. Frequency-multiplexed qubit control reduces the number of control lines needed for qubit manipulation [2–9]. In this architecture, a single control line connects the electronics at room temperature to multiple qubits in the cryogenic environment. Inside the dilution refrigerator, the microwave signal is distributed to individual qubits through a divider, as illustrated in Fig. 1(a). As schematically shown in Fig. 1(b), by allocating qubit frequencies to ensure sufficient detuning relative to achievable Rabi frequencies [7,10,11], it is possible to suppress unwanted excitations of nontarget qubits.

However, this signal distribution can induce off-resonant excitations of nontarget qubits when the detuning is narrower than the pulse bandwidth [Fig. 1(c)], degrading the fidelity of quantum gate operations [12]. Typically, for superconducting qubits, pulse lengths of tens of nanoseconds are used for single-qubit gate operations, resulting in a drive pulse bandwidth in the tens of megahertz range. The bandwidth of typical qubit controllers is around a few gigahertz [8], limiting the multiplexing factor to tens of qubits per control line. At this level of multiplexing, realizing a fault-tolerant quantum processor with millions of qubits would still require approximately $\mathcal{O}(10^5)$ control lines. This already exceeds the physical limitations of the dilution refrigerator [1], implying that the degree of multiplexing is still insufficient.

In this work, we propose a selective-excitation-pulse (SEP) technique to enhance the multiplexing factor of the frequency-multiplexed qubit-control architecture. The SEP technique involves designing a drive pulse that exhibits a frequency profile $S(\omega)$ with null points at the frequencies of nontarget qubits [12–18]. Therefore, the SEP technique enables the selective excitation of target qubits that share a single microwave line, even when the qubit frequencies are densely allocated, as illustrated in Fig. 1(d).

By applying the SEP technique, we experimentally demonstrate the selective excitation of a single qubit out of three using a shared microwave line. We implement single-qubit gates based on the SEP technique and evaluate their performance using randomized benchmarking [19]. The average gate fidelity confirms the effectiveness of the SEP technique. Integrating the SEP technique with the frequency-multiplexed qubit-control architecture enhances the ability to simultaneously control a larger number of qubits using fewer microwave lines. We note that while there is certainly potential for

*These authors contributed equally to this work.
†Contact author: u657789f@ecs.osaka-u.ac.jp
‡Contact author: ohira@quel-inc.com

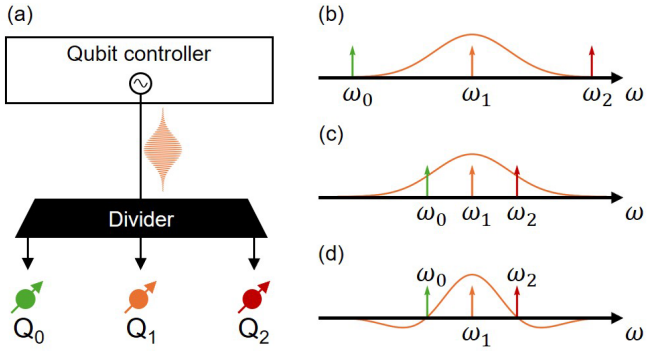

FIG. 1. (a) Frequency-multiplexed qubit-control architecture. Multiple qubits can be manipulated using a single microwave line. (b) Qubit-frequency spacing wider than the bandwidth of the drive pulse. The off-resonant excitation is mitigated. (c) Narrow qubit-frequency spacing. The bandwidth of the drive pulse overlaps with the transition frequencies of nontarget qubits. (d) Selective excitation pulse. The frequency profile of the SEP exhibits null points in the frequency-domain amplitude at the desired frequency. Aligning these null points with the frequencies of nontarget qubits effectively mitigates unwanted excitations.

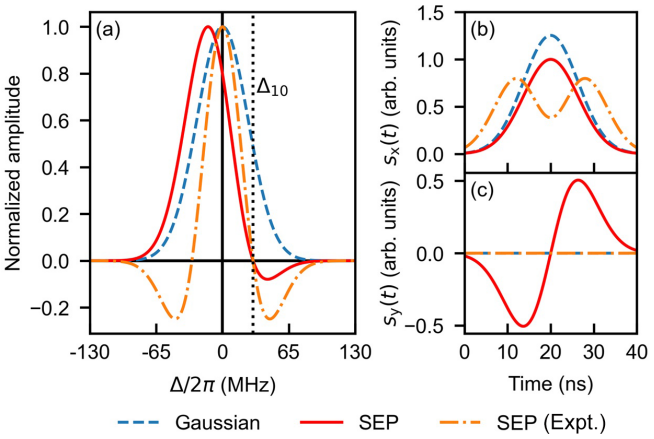

FIG. 2. (a) Frequency profiles of the control pulses. The dashed curve shows the Gaussian profile, the solid curve represents the profile $S_{\mathrm{SEP}}(\omega)$, and the dot-dashed curve corresponds to the profile $S_{\mathrm{Exp}}(\omega)$. Detailed parameters used to plot the frequency profiles are provided in the main text. (b) Real part s_x and (c) imaginary part s_y of the waveforms obtained from the frequency profiles shown in panel (a).

extending the SEP technique to frequency-multiplexed qubit control under conditions of frequency separations comparable to the Rabi frequency, this presents important challenges that warrant further investigation and lie beyond the scope of the present study. In particular, the calibration overhead may increase significantly with the number of qubits sharing a control line.

Selective excitation pulse: Hamiltonian. We now outline the general concept of the SEP technique. Suppose a system comprises N qubits connected to a single microwave line via a divider, as illustrated in Fig. 1(a). In this setup, when the qubits are driven by a microwave pulse at frequency ω_{d}, the Hamiltonian in the rotating frame of the drive frequency is given by

$$\hat{H} = -\frac{1}{2}\sum_j \Delta_j \hat{\sigma}_{j,z} + \frac{1}{2}\sum_j [s_x(t)\hat{\sigma}_{j,x} - s_y(t)\hat{\sigma}_{j,y}], \quad (1)$$

where $\Delta_j = \omega_j - \omega_{\mathrm{d}}$ represents the detuning between the drive frequency ω_{d} and the resonance frequency of the jth qubit ω_j. Here, $\hbar$ is set to 1. The operators $\hat{\sigma}_{j,x}$, $\hat{\sigma}_{j,y}$, and $\hat{\sigma}_{j,z}$ are the Pauli operators for the jth qubit. Additionally, $s_x(t)$ and $s_y(t)$ are the real and imaginary parts of the waveform $s(t)$, respectively. When the detuning Δ_j is small, a drive pulse intended for a target qubit may excite nontarget qubits [Fig. 1(c)].

Selective excitation pulse: Pulse shaping for selective excitation. The essence of the SEP technique involves designing a pulse that exhibits null points at the frequencies of nontarget qubits, thereby preventing their unintended excitation. Let $\mathcal{Q}_{\mathrm{NT}}$ denote the set of nontarget qubits. The frequency profile of the SEP is described by the following equation:

$$S_{\mathrm{SEP}}(\omega) = A\left[\prod_{j\in\mathcal{Q}_{\mathrm{NT}}}(\omega-\omega_j)\right]\exp\left[-\frac{(\omega-\omega_d)^2}{2\sigma^2}\right], \quad (2)$$

where A is the amplitude and σ determines the width of the Gaussian envelope. The frequency of the target qubit is excluded from the product to ensure that the frequency profile does not have a null point at the target qubit frequency.

In the experiment, we employ a slightly modified frequency profile given as follows:

$$S_{\mathrm{Exp}}(\omega) = A\left[\prod_{j\in\mathcal{Q}_{\mathrm{NT}}}(\omega-\omega_j)(\omega-2\omega_{\mathrm{d}}+\omega_j)\right] \times \exp\left[-\frac{(\omega-\omega_{\mathrm{d}})^2}{2\sigma^2}\right]. \quad (3)$$

The correction transforms the frequency profile to be symmetric about the drive frequency ω_{d}, helping to minimize phase shifts due to ac Stark shifts [15].

Now, let us consider a concrete example with two qubits, Q_0 and Q_1, designated as the target qubit and the nontarget qubit, respectively, with frequencies ω_0 and ω_1. The frequency profile of the SEP, designed to suppress excitation in Q_1, is shown in Fig. 2(a). Note that the corresponding frequency profiles are plotted as a function of the detuning Δ relative to the frequency of Q_0. In Fig. 2(a), the solid and the dot-dashed curves represent the frequency profiles based on Eqs. (2) and (3), respectively, with parameters $\sigma/2\pi = 25$ MHz and $\Delta_{10}/2\pi = 30$ MHz. Here, $\Delta_{10} = \omega_1 - \omega_0$ represents the frequency difference between Q_0 and Q_1. Additionally, the frequency profile of a Gaussian pulse is shown as the dashed curve, plotted using Eq. (2) with the nontarget qubit terms set to 1, with a parameter $\sigma/2\pi = 25$ MHz. Note that, for all frequency profiles shown in Fig. 2(a), the amplitude A is set such that the peak of each frequency profile reaches unity.

The corresponding time-domain signal $s(t)$ is then obtained by applying the inverse Fourier transform to the frequency profile:

$$s(t) = \mathcal{F}^{-1}[S(\omega)]. \quad (4)$$

TABLE I. Summary of the qubit and readout parameters.

	Q_0	Q_1	Q_2
Qubit frequency (GHz)	8.895	8.818	8.792
Anharmonicity (MHz)	−411	−433	−413
Energy-relaxation time (μs)	25	18	18
Echo dephasing time (μs)	21	17	18
Readout-resonator frequency (GHz)	10.456	10.466	10.518

The real and imaginary parts of the time-domain signal, obtained from the frequency profiles shown in Fig. 2(a), are shown in Figs. 2(b) and 2(c), respectively. By using these signals to drive the target qubit, we suppress excitations in nontarget qubits [20].

The SEP technique exhibits discontinuities at the initial and final points of the waveform, as shown in Fig. 2(b). These discontinuities can induce spectral leakage and associated control errors. To suppress such effects, the smoothness of the waveform is improved by appropriately tuning the spectral width parameter σ in Eq. (2). A detailed discussion of the origin and mitigation of these discontinuities is provided in Appendix C.

Experimental demonstration of selective-excitation-pulse technique: Experimental setup. To investigate the effectiveness of the SEP technique, we conducted a series of experiments. The experimental setup employed in this study is illustrated in Appendix D. All experiments were conducted using a device consisting of 64 fixed-frequency transmon qubits [21–24]. Our objective was to demonstrate that the SEP technique enables selective excitation even when qubits with closely spaced resonance frequencies are connected to the same microwave line. For this purpose, we required a set of qubits with resonance frequencies within the bandwidth of the drive pulse used in this study. Based on this criterion, we selected three transmon qubits, labeled Q_0, Q_1, and Q_2, respectively. The selected qubits are not nearest neighbors and thus do not have direct couplings between them. The detailed properties of the qubits and their associated resonators used in the experiments are summarized in Table I.

To experimentally demonstrate our proposed technique, we controlled the selected three qubits using a shared microwave line. The microwave signal for qubit control was split into three separate control lines using a power divider, with each line directed to an individual qubit (for more details, see Appendix D). While the primary motivation of this study is to reduce the number of microwave lines inside the dilution refrigerator by installing a divider to split the signal just before reaching the qubits, the current experimental setup is sufficient for a proof-of-concept demonstration.

Experimental demonstration of selective-excitation-pulse technique: Results. In the first experiment, we implemented an $X_{\pi/2}$ gate using the SEP technique and a Gaussian pulse with a duration of 40 ns to assess the suppression of unwanted excitations in nontarget qubits. We calibrated the amplitude A of the frequency profile, given in Eq. (3), to achieve a rotation angle of $\pi/2$. To compensate for phase drift caused by ac Stark shifts during gate operations, we introduced and fine-tuned an additional detuning parameter δ of the frequency profile (see Appendix B). The waveforms used to implement the $X_{\pi/2}$ gate and their parameters are provided in the Appendixes.

Using the SEP technique and Gaussian pulses, we repeatedly applied the $X_{\pi/2}$ gates to the three qubits and measured the population of each qubit. We executed 1000 experiments to obtain P_g, the probability of finding the qubit in its ground state. After each measurement, we waited for a period of at least $10T_1$ to ensure that the qubit state was properly initialized.

In Fig. 3, we present the Rabi oscillations under repeated $X_{\pi/2}$ gates. As shown in Figs. 3(a), 3(e), and 3(i), the $X_{\pi/2}$ gate is properly calibrated using both the SEP and Gaussian pulses.

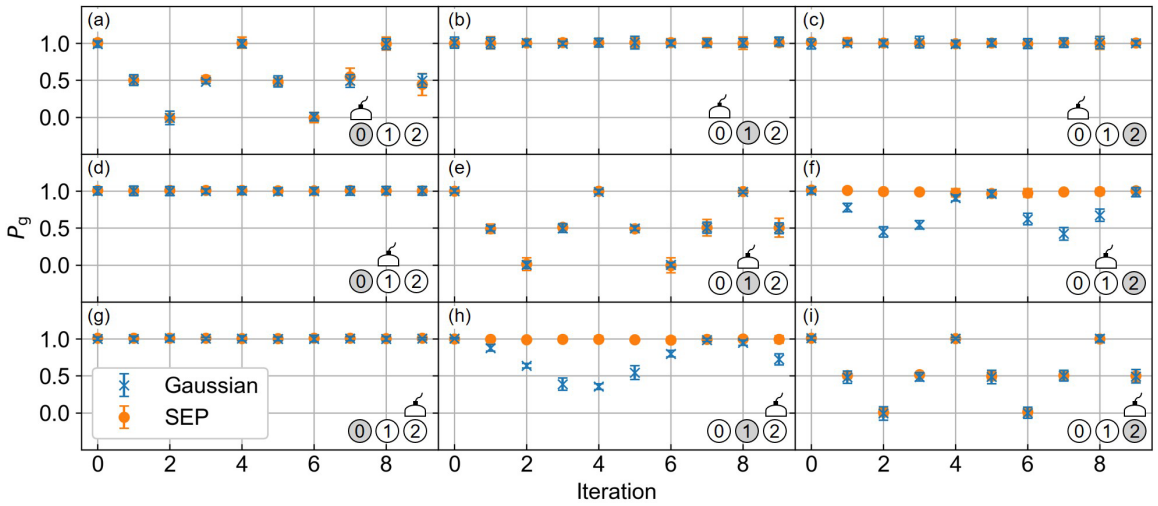

FIG. 3. Rabi oscillations observed when applying repeated $X_{\pi/2}$ gates using Gaussian pulses (crosses) and the SEPs (dots). Measured results for (a)–(c)Q_0, (d)–(f) Q_1, and (g)–(i) Q_2. Each data point represents the average of five experiments, with error bars indicating 1σ confidence intervals. In insets, the target qubit is shown in gray, and the nontarget qubits are shown in white. The detector icon indicates the qubit that was measured to obtain the results.

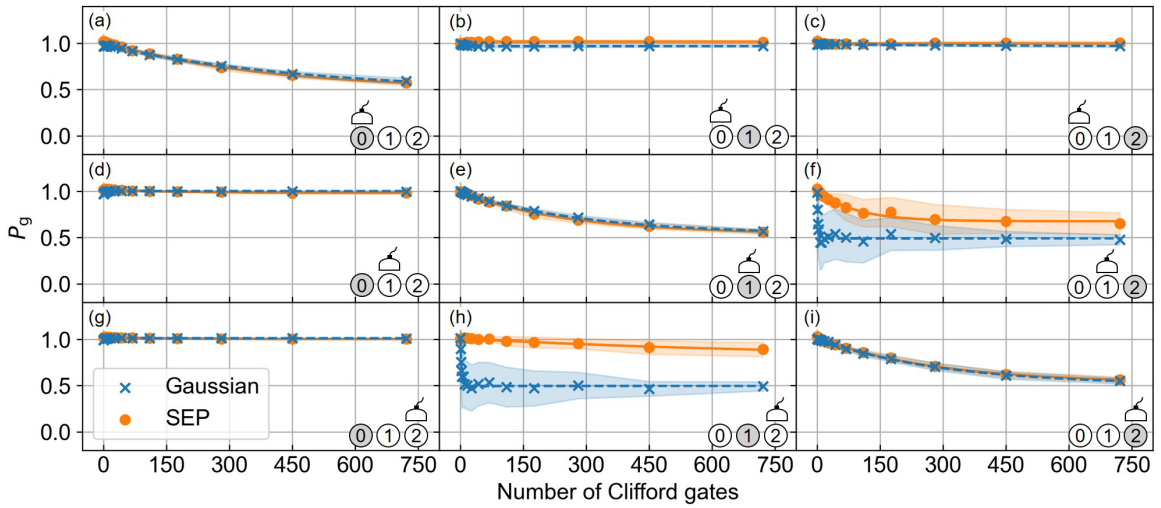

FIG. 4. Randomized benchmarking of single-qubit gates for Gaussian pulses (crosses) and the SEPs (dots). Measured results for (a)–(c) Q_0, (d)–(f) Q_1, and (g)–(i) Q_2. Data points represent the average of 50 different random Clifford sequences, with shaded regions indicating the standard deviation across the 50 results for each Clifford-gate number. The $X_{\pi/2}$ gate was calibrated in the SEP technique. The SEP technique achieved an average gate fidelity comparable to that of Gaussian pulses.

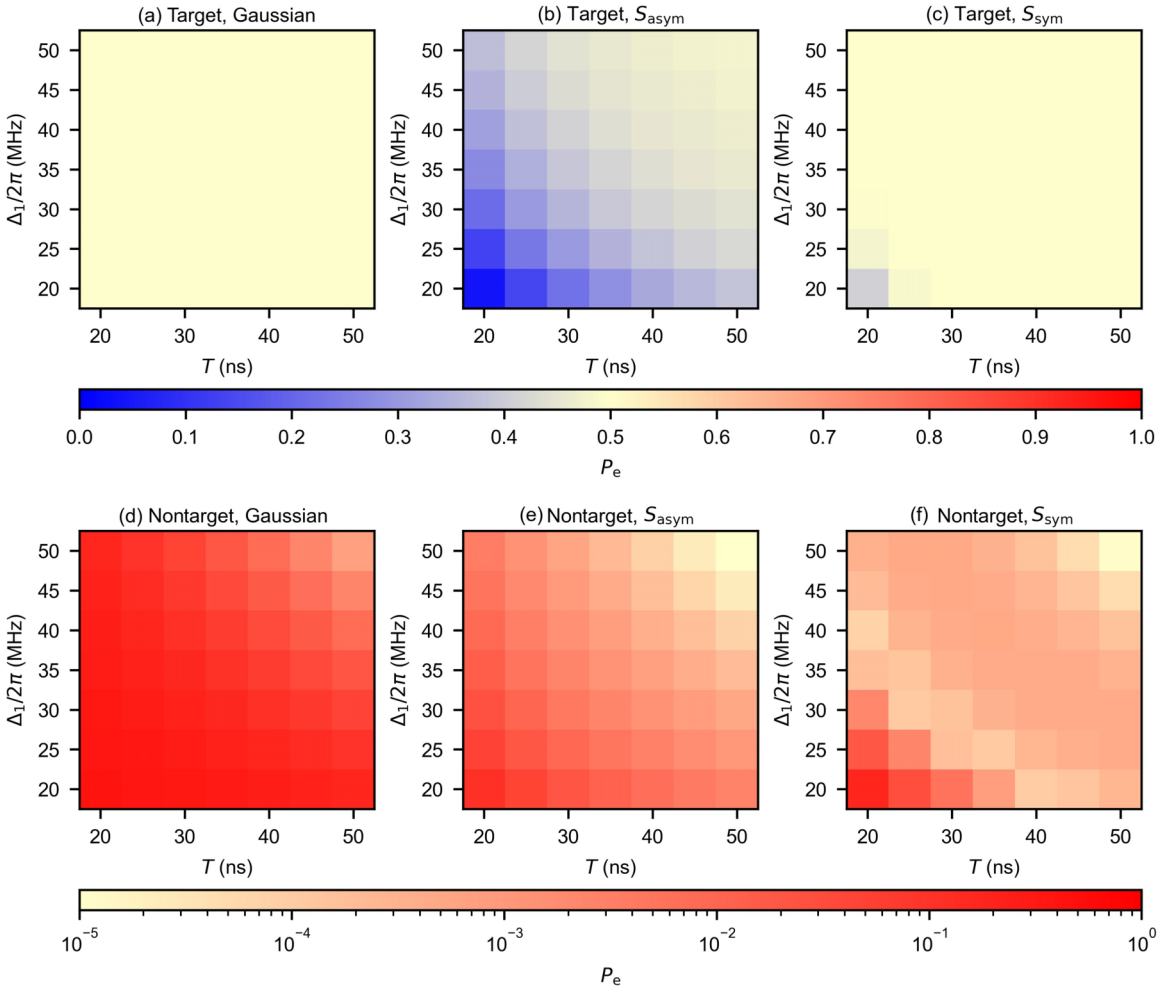

FIG. 5. Numerical simulation of the excitation probability P_e of the target qubit Q_0 and the nontarget qubit Q_1 after an $X_{\pi/2}$ gate, shown as a function of the pulse duration T and detuning Δ_1. Results for Q_0 using three waveform types: (a) Gaussian, (b) $s_{asym}(t)$, and (c) $s_{sym}(t)$. (d)–(f) Results for Q_1, using the same waveform types as in panels (a)–(c).

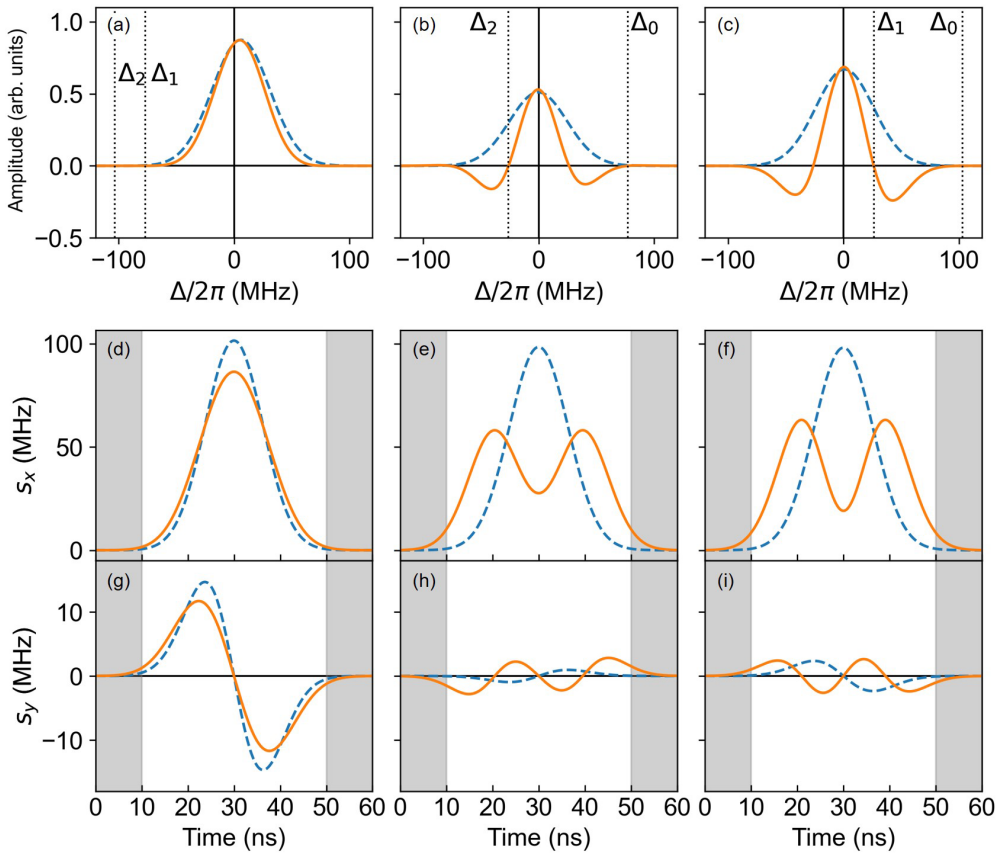

FIG. 6. Frequency profiles and time-domain signals used to implement the $X_{\pi/2}$ gates. (a)–(c) Frequency profiles for the target qubits Q_0, Q_1, and Q_2, respectively. The dashed and solid curves show the results for Gaussian pulses and the SEPs, respectively. Time-domain signals derived from each frequency profile: (d)–(f) real parts s_x and (g)–(i) imaginary parts s_y of the corresponding waveforms. The shaded regions indicate truncated segments of the waveforms and the nonshaded regions indicate the waveforms used in the experiments.

Off-resonant excitations are observed in the nontarget qubits when Gaussian pulses are used, as illustrated in Figs. 3(f) and 3(h). In contrast, the SEP technique effectively suppresses these unwanted excitations.

Next, to evaluate the average fidelity of the single-qubit gate using the SEP technique, we performed single-qubit randomized benchmarking [19]. All single-qubit Clifford gates were composed of $X_{\pi/2}$ gates and virtual-Z gates [25]. For comparison, we also evaluated the single-qubit gate fidelity using Gaussian pulses. Figures 4(a), 4(e), and 4(i) present the results of the single-qubit randomized benchmarking. Using the single-qubit gate with the SEP technique, the average single-qubit Clifford gate fidelities were determined to be 99.87(1)%, 99.80(2)%, and 99.82(2)% for target qubits Q_0, Q_1, and Q_2, respectively. In comparison, the Gaussian pulses yielded fidelities of 99.90(2)%, 99.83(2)%, and 99.83(1)% for Q_0, Q_1, and Q_2, respectively. The fidelities achieved with the SEP technique are thus comparable to those obtained with Gaussian pulses.

In addition to the gate fidelity, we examined the excitation probability for nontarget qubits to quantify unwanted excitations. We fit the populations P_g to a decay model $Ap^L + B$, where p is the depolarizing rate. Here, the coefficients A and B account for state preparation errors and the asymptotic population value as the sequence length increases.

The obtained results for nontarget qubits are shown in Figs. 4(f) and 4(h). There is a clear difference in the excitation levels between experiments using the SEP technique and those using Gaussian pulses. To quantify this difference in off-resonant excitation between the SEP technique and Gaussian pulses, we introduce the excitation rate, defined as $\Gamma_{\mathrm{ex}} \equiv B(1-p)/2$. Physically, this rate reflects the balance between state excitation and energy relaxation over the sequence length.

Conclusion and discussion. Based on the results shown in Fig. 4(f) [Fig. 4(h)], the excitation rate is 0.2% (0.01%) for the SEP technique and 10% (7%) for Gaussian pulses. These results indicate that using the SEP technique effectively suppresses excitations compared to Gaussian pulses. Although Gaussian pulses are used as the base pulse in this study, the SEP technique is compatible with other basis-pulse shapes, including raised-cosine pulses. Additionally, SEP may be compatible with techniques such as the derivative removal by adiabatic gate [20,26]. We numerically explored this possibility and found that the combination can suppress leakage to the order of 10^{-4} with parameters: a pulse duration $T = 16$ ns, the detuning between the target qubit and the nontarget qubit 46 MHz, and an anharmonicity $\alpha/2\pi = -300$ MHz, potentially enabling faster and more robust gate implementations.

In this work, we demonstrated the selective control of three transmon qubits through a single microwave line by

TABLE II. Parameters used for the Gaussian pulses and the SEPs.

	Gaussian pulse			SEP		
Target qubit	Q_0	Q_1	Q_2	Q_0	Q_1	Q_2
$\delta/2\pi$ (MHz)	6.019	−0.3979	0.9885	6.561	−1.767	1.354
$\Delta_j/2\pi$ (MHz)	–	–	–	−77	77	103
$\Delta_j/2\pi$ (MHz)				−103	−26	26
$\omega_d/2\pi$ (GHz)	8.895	8.818	8.792	8.895	8.818	8.792
$\sigma/2\pi$ (MHz)	25	25	25	25	25	25

leveraging the SEP technique. We achieved gate fidelities comparable to Gaussian-pulse-based operations while significantly suppressing unwanted excitations in nontarget qubits. Our results suggest that the SEP technique can serve as a valuable tool for implementing efficient, scalable qubit control in advanced quantum computing architectures. Our work addresses the challenge of selectively controlling qubits whose resonant frequencies are closely spaced. The SEP technique allows individual addressing without disturbing neighboring qubits, but it does not itself provide simultaneous multiqubit operations. In future work, the SEP approach can be combined with time-division multiplexing [27,28] or extended toward simultaneous gate implementation on a shared control line.

Acknowledgments. This research was supported by JST COI-NEXT (Grant No. JPMJPF2014), JST Moonshot R&D (Grants No. JPMJMS2067 and No. JPMJMS226A), MEXT Q-LEAP (Grant No. JPMXS0118068682), JST PRESTO (Grant No. JPMJPR23F2), and JST the establishment of university fellowships toward the creation of science technology innovation (Grant No. JPMJSP2138).

Data availability. The data that support the findings of this article are not publicly available. The data are available from the authors upon reasonable request.

Appendix A: Suppression of unintended excitation using selective excitation pulse. To illustrate how a drive pulse based on the SEP technique suppresses unintended excitation, we analyze the dynamics of a nontarget qubit under the Hamiltonian given by

$$\hat{H} = \sum_j \Delta_j \hat{a}_j^\dagger \hat{a}_j + \frac{1}{2}\sum_j [s(t)\hat{a}_j^\dagger + s^*(t)\hat{a}_j], \tag{A1}$$

where $\Delta_j = \omega_j - \omega_d$ represents the detuning between the drive frequency ω_d and the resonance frequency of the jth qubit ω_j. $\hat{a}_j^\dagger$ ($\hat{a}_j$) denotes the creation (annihilation) operator of the jth qubit. $s(t)$ indicates an envelope of pulse used to drive qubits. Note that we set $\hbar = 1$.

Here, we consider a situation with two qubits: the target qubit Q_0 and the nontarget qubit Q_1 with respective frequencies ω_0 and ω_1. Both qubits are initially prepared in the ground state $|g\rangle$. Although our analysis focuses on a two-qubit

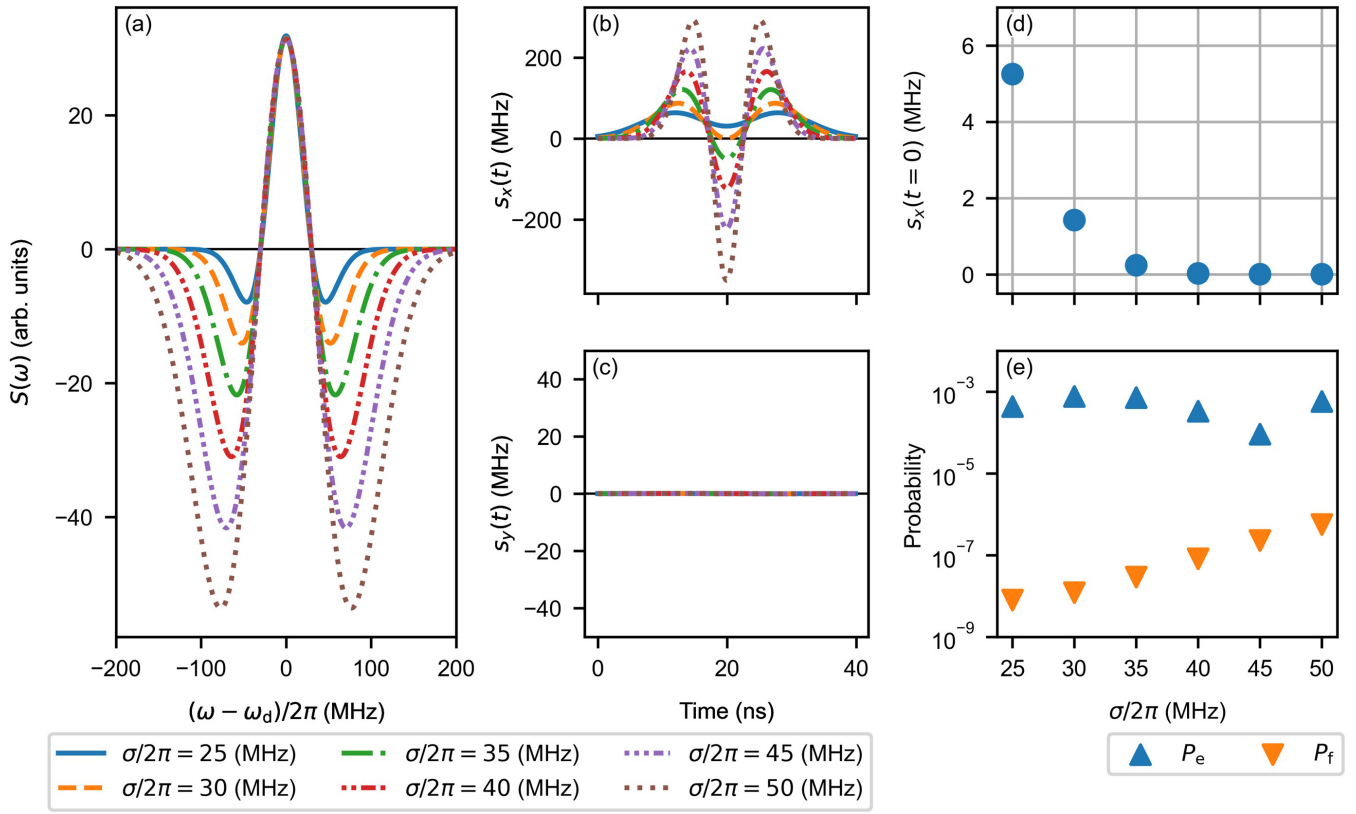

FIG. 7. Analysis of the waveform discontinuity. (a) Frequency profiles of the SEP given by Eq. (A3), with the amplitudes normalized so that $s(t)$ satisfies the area condition $\int_0^T s(t)\,dt = \pi/2$. Here, $s(t)$ is obtained via the inverse Fourier transform of $S(\omega)$ in panel (a). (b), (c) Time-domain signals: real part $s_x(t)$ and imaginary part $s_y(t)$ of the waveform $s(t)$. (d) Value of $s_x(t=0)$ as a function of σ, showing the discontinuity due to the truncation. (e) Numerical results of P_e (P_f), the probability of projecting the nontarget qubit into the first (second) excited state $|e\rangle$ ($|f\rangle$).

system for clarity, the SEP technique and its suppression of unintended excitations can be generalized to systems with n qubits.

Using the Hamiltonian and the three types of waveforms, we calculate P_e, the probability of finding the nontarget qubit in the first excited state $|e\rangle$ after a pulse duration of T. The first waveform is a Gaussian pulse, while the second and third waveforms are derived from the following frequency profiles:

$$S_{\text{asym}}(\omega) = A(\omega - \omega_1)\exp\left[-\frac{(\omega-\omega_d)^2}{2\sigma^2}\right] \tag{A2}$$

and

$$S_{\text{sym}}(\omega) = A(\omega-\omega_1)(\omega - 2\omega_d + \omega_1) \times \exp\left[-\frac{(\omega-\omega_d)^2}{2\sigma^2}\right]. \tag{A3}$$

Here, A is the amplitude and σ determines the width of the Gaussian envelope. The parameters used for this calculation are $\sigma/2\pi = 1/T$. The amplitude A and the drive frequency ω_d are chosen to satisfy $\int_0^T s_{\text{asym (sym)}}(t)\,dt = \pi/2$ and $\Delta_0 = 0$, where $s_{\text{asym (sym)}}(t)$ is, respectively, obtained by applying the inverse Fourier transform to $S_{\text{asym (sym)}}(\omega)$, followed by truncation within the pulse duration T.

Figure 5 summarizes P_e as functions of the pulse duration T and the detuning Δ_1. Figures 5(a)–5(c) show the excitation probability of the target qubit Q_0 driven by different pulses: Gaussian pulse [Fig. 5(a)], SEP $s_{\text{asym}}(t)$ [Fig. 5(b)], and SEP $s_{\text{sym}}(t)$ [Fig. 5(c)]. Figures 5(d)–5(f) show the corresponding excitation probability P_e for the nontarget qubit Q_1. For the target qubit Q_0, the Gaussian pulse [Fig. 5(a)] achieves $P_e > 0.49$ with relatively short durations (approximately 20 ns), while SEP-based pulses [Figs. 5(b) and 5(c)] generally require longer durations to reach similar excitation levels. In contrast, for the nontarget qubit Q_1, SEP-based pulses [Figs. 5(e) and 5(f)] provide significantly better suppression of unwanted excitation than the Gaussian pulse [Fig. 5(d)], particularly when the detuning Δ_1 is small. These results indicate that by utilizing the SEP technique, selective excitation of the target qubit can be achieved even when the frequencies of the target and nontarget qubits are closely spaced.

Appendix B: Selective excitation pulse for single-qubit gate operation. The frequency profile for implementing an $X_{\pi/2}$ gate using the SEP technique in the experiment is given as follows:

$$S(\omega) = A\left[\prod_{j\in\mathcal{Q}_{\text{NT}}}(\omega-\omega_j)(\omega-2\omega_d+\omega_j)\right] \times \exp\left[-\frac{(\omega-\omega_d-\delta)^2}{2\sigma^2}\right]. \tag{B1}$$

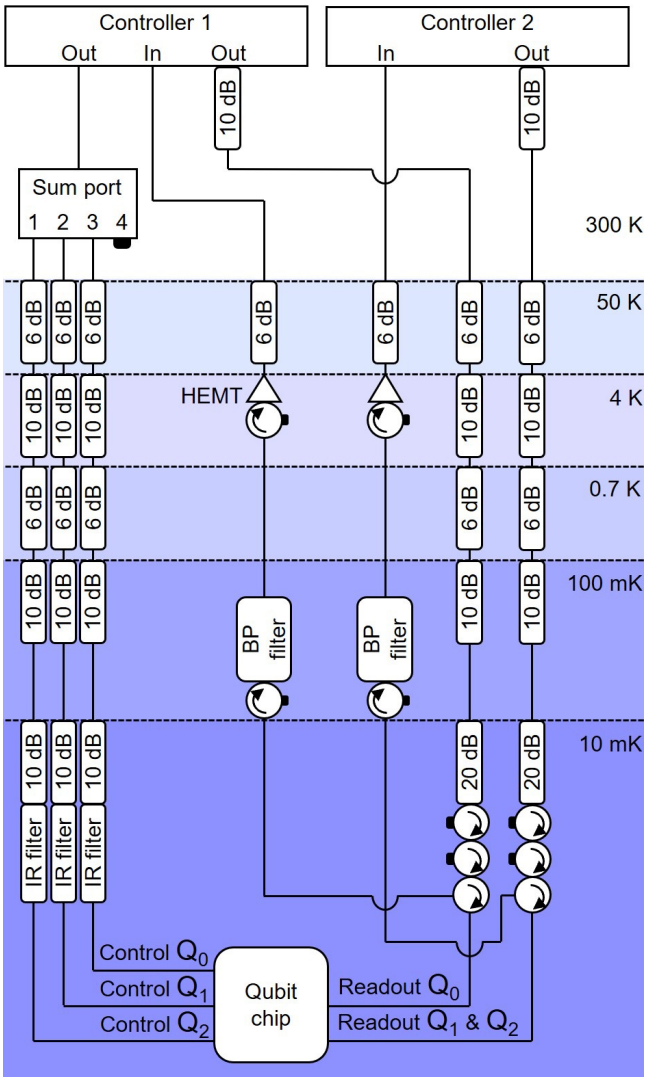

FIG. 8. Wiring schematic of the experimental setup. Background color indicates the temperature at each stage. The setup allows pulses driving the target qubit to interact with nontarget qubits via a signal divider.

Here, the detuning parameter δ is introduced to further fine-tune the frequency profile. By adjusting δ, we compensate for residual ac Stark shifts during gate operations [15].

The waveforms corresponding to the $X_{\pi/2}$ gate are shown in Fig. 6, and the detailed parameters are summarized in Table II.

Appendix C: Discontinuities in the selective excitation pulse. Due to the finite temporal duration of the waveform, SEPs exhibit discontinuities at their start and end points, as shown in Fig. 6. These discontinuities are expected to introduce significant spectral leakage, particularly for shorter pulses where truncation effects become more pronounced. To mitigate this issue and improve waveform smoothness, we investigate the role of the spectral width parameter σ in Eq. (A3), which defines the envelope width of the frequency-domain profile. The amplitude A is normalized such that the time-domain waveform $s(t)$, obtained via inverse Fourier

transform of $S(\omega)$, satisfies the area condition $\int_0^T s(t)\,dt = \pi/2$, with a fixed truncated pulse duration $T = 40$ ns. We set $\Delta_1/2\pi = 0.03$ GHz, where Δ_1 denotes the detuning between the drive frequency ω_d and the nontarget frequency ω_1 in Eq. (A3).

To examine the influence of σ, we compute the frequency-domain profiles $S(\omega)$ and the corresponding time-domain waveforms $s(t)$ for several values of $\sigma/2\pi$, as shown in Figs. 7(a)–7(c). The time-domain signals reveal that both the initial and final points of the waveform become smoother as σ increases. To quantify this effect, Fig. 7(d) plots the real part $s_x(t = 0)$ as a function of σ. The amplitude at the initial time point decreases as $\sigma/2\pi$ increases, indicating the reduction in discontinuity. Finally, for each $s(t)$ as shown in Figs. 7(b) and 7(c), we numerically determine P_e (P_f), the probability of projecting the nontarget qubit into the first (second) excited state $|e\rangle$ ($|f\rangle$) after driven by each pulse, as a function of σ. The unwanted excitation P_e of the nontarget qubit is suppressed at a level of 10^{-4} for any value of σ. Although the reduction of the discontinuity is shown in Fig. 7(e), increasing the microwave amplitude as shown in Fig. 7(b) leads to the unintended excitation P_e and the leakage P_f of the nontarget qubits.

Appendix D: Measurement setup. The experimental setup employed in this study is illustrated in Fig. 8. The device consisting of 64 fixed-frequency transmon qubits was mounted to the stage of a dilution refrigerator (Bluefors XLD1000sl) at approximately 10 mK and was magnetically shielded.

All microwave signals for qubit control and readout were generated by qubit controllers (QuEL, Inc.) [24,29]. These signals were routed to the qubits via attenuators placed at the various stages of the dilution refrigerator.

The qubit readout was performed using a dispersive readout technique [30]. The readout resonator in the device was dispersively coupled to one of the four transmon qubits in a unit cell, allowing for the simultaneous readout of all four qubits. In this setup, Q_1 and Q_2 shared the same measurement line. The readout signals were amplified by high-electron-mobility transistor amplifiers located at the 4-K stage before being routed back to the qubit controllers.

[1] S. Krinner, S. Storz, P. Kurpiers, P. Magnard, J. Heinsoo, R. Keller, J. Lütolf, C. Eichler, and A. Wallraff, Engineering cryogenic setups for 100-qubit scale superconducting circuit systems, EPJ Quantum Technol. **6**, 2 (2019).

[2] R. Huang, X. Geng, X. Wu, G. Dai, L. Yang, J. Liu, and W. Chen, Cryogenic multiplexing control chip for a superconducting quantum processor, Phys. Rev. Appl. **18**, 064046 (2022).

[3] N. Takeuchi, T. Yamae, W. Luo, F. Hirayama, T. Yamamoto, and N. Yoshikawa, Scalable flux controllers using adiabatic superconductor logic for quantum processors, Phys. Rev. Res. **5**, 013145 (2023).

[4] N. Takeuchi, T. Yamae, T. Yamashita, T. Yamamoto, and N. Yoshikawa, Microwave-multiplexed qubit controller using adiabatic superconductor logic, npj Quantum Inf. **10**, 53 (2024).

[5] P. Shi, J. Yuan, F. Yan, and H. Yu, Multiplexed control scheme for scalable quantum information processing with superconducting qubits, arXiv:2312.06911.

[6] P. Zhao, R. Wang, M.-J. Hu, T. Ma, P. Xu, Y. Jin, and H. Yu, Baseband control of superconducting qubits with shared microwave drives, Phys. Rev. Appl. **19**, 054050 (2023).

[7] J. P. G. van Dijk, E. Kawakami, R. N. Schouten, M. Veldhorst, L. M. K. Vandersypen, M. Babaie, E. Charbon, and F. Sebastiano, Impact of classical control electronics on qubit fidelity, Phys. Rev. Appl. **12**, 044054 (2019).

[8] J. P. G. Van Dijk, *et al.*, A scalable cryo-CMOS controller for the wideband frequency-multiplexed control of spin qubits and transmons, IEEE J. Solid-State Circuits **55**, 2930 (2020).

[9] R. Ohira, R. Matsuda, H. Shiomi, K. Ogawa, and M. Negoro, Optimizing multi-tone microwave pulses via phase selection for quantum computing applications, J. Appl. Phys. **136**, 114402 (2024).

[10] A. R. Mills, C. R. Guinn, M. J. Gullans, A. J. Sigillito, M. M. Feldman, E. Nielsen, and J. R. Petta, Two-qubit silicon quantum processor with operation fidelity exceeding 99%, Sci. Adv. **8**, eabn5130 (2022).

[11] W. I. L. Lawrie, M. Rimbach-Russ, F. van Riggelen, N. W. Hendrickx, S. L. d. Snoo, A. Sammak, G. Scappucci, J. Helsen, and M. Veldhorst, Simultaneous single-qubit driving of semiconductor spin qubits at the fault-tolerant threshold, Nat. Commun. **14**, 3617 (2023).

[12] L. M. K. Vandersypen and I. L. Chuang, NMR techniques for quantum control and computation, Rev. Mod. Phys. **76**, 1037 (2005).

[13] N. Linden, Ē. Kupče, and R. Freeman, NMR quantum logic gates for homonuclear spin systems, Chem. Phys. Lett. **311**, 321 (1999).

[14] F. Motzoi, J. M. Gambetta, P. Rebentrost, and F. K. Wilhelm, Simple pulses for elimination of leakage in weakly nonlinear qubits, Phys. Rev. Lett. **103**, 110501 (2009).

[15] Z. Chen, *et al.*, Measuring and suppressing quantum state leakage in a superconducting qubit, Phys. Rev. Lett. **116**, 020501 (2016).

[16] E. Hyyppä, A. Vepsäläinen, M. Papič, C. F. Chan, S. Inel, A. Landra, W. Liu, J. Luus, F. Marxer, C. Ockeloen-Korppi, S. Orbell, B. Tarasinski, and J. Heinsoo, Reducing leakage of single-qubit gates for superconducting quantum processors using analytical control pulse envelopes, PRX Quantum **5**, 030353 (2024).

[17] K. Yi, Y.-J. Hai, K. Luo, J. Chu, L. Zhang, Y. Zhou, Y. Song, S. Liu, T. Yan, X.-H. Deng, Y. Chen, and D. Yu, Robust quantum gates against correlated noise in integrated quantum chips, Phys. Rev. Lett. **132**, 250604 (2024).

[18] Z. H. Yang, R. Wang, Z. T. Wang, P. Zhao, K. Huang, K. Xu, Y. Tian, H. F. Yu, and S. P. Zhao, Mitigation of microwave crosstalk with parameterized single-qubit gate in superconducting quantum circuits, Appl. Phys. Lett. **124**, 214001 (2024).

[19] E. Magesan, J. M. Gambetta, and J. Emerson, Scalable and robust randomized benchmarking of quantum processes, Phys. Rev. Lett. **106**, 180504 (2011).

[20] F. Motzoi and F. K. Wilhelm, Improving frequency selection of driven pulses using derivative-based transition suppression, Phys. Rev. A **88**, 062318 (2013).

[21] J. Koch, T. M. Yu, J. Gambetta, A. A. Houck, D. I. Schuster, J. Majer, A. Blais, M. H. Devoret, S. M. Girvin, and R. J. Schoelkopf, Charge-insensitive qubit design derived from the Cooper pair box, Phys. Rev. A **76**, 042319 (2007).

[22] S. Tamate, Y. Tabuchi, and Y. Nakamura, Toward realization of scalable packaging and wiring for large-scale superconducting quantum computers, IEICE Trans. Electron. **E105.C**, 290 (2022).

[23] S. Watanabe, Y. Tabuchi, K. Heya, S. Tamate, and Y. Nakamura, *ZZ*-interaction-free single-qubit-gate optimization in superconducting qubits, Phys. Rev. A **109**, 012616 (2024).

[24] M. Negoro, K. Ogawa, T. Miyoshi, H. Shiomi, S. Morisaka, R. Matsuda, K. Koike, S. Funada, R. Ohira, T. Sumida, Y. Kurimoto, Y. Sugita, Y. Ito, Y. Suzuki, P. A. Spring, S. Wang, S. Tamate, Y. Tabuchi, and Y. Nakamura, Experimental demonstrations of broadband quantum control of superconducting qubits with QuBE (qubit-controller with broadband electronics), in APS March Meeting, Minneapolis (2024), D49.00005.

[25] D. C. McKay, C. J. Wood, S. Sheldon, J. M. Chow, and J. M. Gambetta, Efficient *Z* gates for quantum computing, Phys. Rev. A **96**, 022330 (2017).

[26] R. Wang, Y. Feng, Y. Zhang, J. Ding, B. Li, F. Motzoi, Y. Gao, H. Xu, Z. Yang, W. Nuerbolati, H. Yu, W. Sun, and F. Yan, Suppressing spurious transitions using spectrally balanced pulse, Phys. Rev. Lett. **135**, 160804 (2025).

[27] R. Acharya, S. Brebels, A. Grill, J. Verjauw, T. Ivanov, D. P. Lozano, D. Wan, J. Van Damme, A. M. Vadiraj, M. Mongillo, B. Govoreanu, J. Craninckx, I. P. Radu, K. De Greve, G. Gielen, F. Catthoor, and A. Potočnik, Multiplexed superconducting qubit control at millikelvin temperatures with a low-power cryo-CMOS multiplexer, Nat. Electron. **6**, 900 (2023).

[28] M. Richter, I. Strandberg, S. Gasparinetti, and A. F. Kockum, Overhead in quantum circuits with time-multiplexed qubit control, arXiv:2508.20752.

[29] T. Sumida, M. Negoro, K. Ogawa, T. Miyoshi, H. Shiomi, S. Morisaka, R. Matsuda, K. Koike, S. Funada, R. Ohira, Y. Kurimoto, Y. Sugita, Y. Ito, Y. Suzuki, P. A. Spring, S. Wang, S. Tamate, Y. Tabuchi, and Y. Nakamura, QuBE: A qubit-controller with broadband electronics, in APS March Meeting, Minneapolis (2024), D49.00004.

[30] A. Blais, R.-S. Huang, A. Wallraff, S. M. Girvin, and R. J. Schoelkopf, Cavity quantum electrodynamics for superconducting electrical circuits: An architecture for quantum computation, Phys. Rev. A **69**, 062320 (2004).